Infrasonic interferometry of stratospherically refracted microbaroms—A numerical study

Julius T. Fricke[a)]
Seismology Division, Royal Netherlands Meteorological Institute, Wilhelminalaan 10, 3732 GK De Bilt, The Netherlands

Nihed El Allouche and Dick G. Simons
Acoustic Remote Sensing Group, Faculty of Aerospace Engineering, Delft University of Technology, Kluyverweg 1, 2629 HS Delft, The Netherlands

Elmer N. Ruigrok and Kees Wapenaar
Department of Geoscience and Engineering, Faculty of Civil Engineering and Geosciences, Delft University of Technology, Stevinweg 1, 2628 CN Delft, The Netherlands

Läslo G. Evers[b)]
Seismology Division, Royal Netherlands Meteorological Institute, Wilhelminalaan 10, 3732 GK De Bilt, the Netherlands

(Received 19 October 2012; revised 18 July 2013; accepted 9 August 2013)

The atmospheric wind and temperature can be estimated through the traveltimes of infrasound between pairs of receivers. The traveltimes can be obtained by infrasonic interferometry. In this study, the theory of infrasonic interferometry is verified and applied to modeled stratospherically refracted waves. Synthetic barograms are generated using a raytracing model and taking into account atmospheric attenuation, geometrical spreading, and phase shifts due to caustics. Two types of source wavelets are implemented for the experiments: blast waves and microbaroms. In both numerical experiments, the traveltimes between the receivers are accurately retrieved by applying interferometry to the synthetic barograms. It is shown that microbaroms can be used in practice to obtain the traveltimes of infrasound through the stratosphere, which forms the basis for retrieving the wind and temperature profiles. © *2013 Acoustical Society of America*. [http://dx.doi.org/10.1121/1.4819117]

PACS number(s): 43.28.Dm, 43.28.En, 43.28.Js [RMW] Pages: 2660–2668

I. INTRODUCTION

In 1996 the Comprehensive Nuclear-Test-Ban Treaty Organization chose the measurements of infrasound as one of its verification techniques. Ever since, the study of infrasound has experienced a renaissance (Dahlman *et al.*, 2009). The treaty is verified through the International Monitoring System, which uses, in addition to the infrasound recordings, seismic, hydroacoustic, and radionuclide measurements.

The traveltimes of infrasound through the atmosphere and their detectability strongly depend on the temperature and the wind in the stratosphere (Gutenberg, 1939). As a consequence of this dependency, temperature and wind profiles can be estimated by measuring the traveltimes of infrasound. For such an estimation, an inversion of the model of infrasound propagation through the atmosphere is required. Numerical studies for building such an inverse model of the atmosphere are done by Drob *et al.* (2010) and Lalande *et al.* (2012).

Accurate traveltimes are an essential input for the inverse model, since small changes in traveltime can lead to large changes in output (temperature and wind). Usually, the traveltimes are measured by a ground-truth event, e.g., an explosion (Evers *et al.*, 2012) or a volcanic eruption (Le Pichon *et al.*, 2005). This dependency on a ground-truth event has the disadvantage that the exact time and location of the event need to be known. Another disadvantage is the very limited occurrence of ground-truth events.

The traveltimes can also be estimated using a method called infrasonic interferometry. This is based on the theory of nonreciprocal Green's function retrieval by crosscorrelation (Wapenaar, 2006; Godin, 2006). This theory determines the outcome of the crosscorrelation of the measured noise field at two receivers A and B in a moving medium. Assuming the noise field is equipartitioned, this crosscorrelation converges to the Green's function from receiver A to receiver B plus the time-reversed Green's function from receiver B to receiver A, convolved with the autocorrelation of the noise. In other words, the traveltimes between two receivers can be determined by crosscorrelating the ambient noise at these two receivers.

The interferometry of acoustic and elastic waves has successfully been applied in oceanography (Roux and Kuperman, 2004), in seismology (Shapiro and Campillo, 2004; Sabra *et al.*, 2005; Bensen *et al.*, 2007; Draganov *et al.*,

a)Author to whom correspondence should be addressed. Also at: The Acoustic Remote Sensing Group, Faculty of Aerospace Engineering, Delft University of Technology, Kluyverweg 1, 2629 HS Delft, The Netherlands. Electronic mail: fricke@knmi.nl
b) Also at: The Department of Geoscience and Engineering, Faculty of Civil Engineering and Geosciences, Delft University of Technology, Stevinweg 1, 2628 CN Delft, The Netherlands.

2007), and in ultrasonic applications (Weaver and Lobkis, 2001).

In a first study with direct tropospheric waves, Haney (2009) has shown that interferometry can also be applied to infrasonic ambient noise. Haney retrieves the temperature and the strength of the wind in the troposphere by using this method. Marcillo and Johnson (2010) have demonstrated that the wind vector can also be resolved by applying interferometry to three infrasound sensors. The ambient infrasonic fluctuations consist mostly of microbaroms (Posmentier, 1967). Microbaroms result from the nonlinear interaction of oceanic waves. Microbaroms are almost continuously present at a frequency of 0.2 Hz (Brekhovskikh *et al.*, 1973; Donn and Naini, 1973).

In this numerical study, infrasonic interferometry is applied to stratospherically refracted microbaroms. With this approach, the traveltimes of infrasound through the stratosphere are obtained. Observations of temperature and wind above an altitude of 20 km are very limited. Therefore, successful application of the interferometric technique to stratospheric infrasound will have a direct use for the validation of upper atmospheric models.

The first part of this paper discusses the theoretical background of interferometry. In the second part, a detailed description of the applied model is given. The third part presents the results of the interferometry applied to numerical data which are generated with the model.

II. INFRASONIC INTERFEROMETRY

In this paper, interferometry is applied to stratospherically refracted infrasound. A derivation of the interferometric relations is given by Wapenaar (2006), which we will summarize in this section.

The atmosphere through which the infrasound propagates is a moving medium. In the aforementioned paper it is shown how interferometry can be used in such a moving medium, under the assumption that the flow velocity of the medium is small in comparison to the sound speed. For higher Mach numbers this approach becomes less accurate for amplitudes, but it still predicts the traveltimes very well. The Green's function between two receivers can be expressed as

$$G(\mathbf{x}_B, \mathbf{x}_A, t) + G(\mathbf{x}_A, \mathbf{x}_B, -t) \approx \frac{2}{\rho c} \oint_S G(\mathbf{x}_A, \mathbf{x}, -t) * G(\mathbf{x}_B, \mathbf{x}, t)\, d^2\mathbf{x}, \quad (1)$$

where the asterisk ($*$) denotes a temporal convolution. Convolved are $G(\mathbf{x}_A, \mathbf{x}, -t)$, the time-reversed Green's function from a source at $\mathbf{x}$ to receiver A (at $\mathbf{x}_A$), with $G(\mathbf{x}_B, \mathbf{x}, t)$, the Green's function from the same source to receiver B (at $\mathbf{x}_B$). The surface integral ($\oint_S$) integrates along all sources $\mathbf{x}$ on boundary surface S of the volume in which the two receivers A and B are located. $G(\mathbf{x}_B, \mathbf{x}_A, t)$ represents the Green's function of infrasound propagation from receiver A to receiver B, and $G(\mathbf{x}_A, \mathbf{x}_B, -t)$ is the time-reversed Green's function of propagation in the opposite direction. Equation (1) holds for inhomogeneous density $\rho(\mathbf{x})$, sound speed $c(\mathbf{x})$, and wind velocity $\vec{u}(\mathbf{x})$ inside surface S. At and outside S the medium is assumed to be homogeneous [denoted by c and ρ in Eq. (1)] and the wind velocity is assumed to be small in comparison with the sound speed. In the case discussed in this paper, the receivers are located on the ground and the waves reach them through the atmosphere. We consider the ground as a totally reflecting (rigid) surface. Since the normal component of the particle velocity on the rigid surface is zero, the integrand of the representation integral underlying Eq. (1) vanishes on the ground surface (Wapenaar and Fokkema, 2006) [see Fig. 1(a)]. Thus, the integration in Eq. (1) over a closed surface can be replaced by an integration over only the upper hemisphere. Equation (1) is valid for both two and three dimensions, but here we will proceed with a two dimensional configuration. Therefore the integration over a hemisphere is reduced to an integration over the semicircle L [see Fig. 1(b)].

Hence, the integration over the sources on the semicircle L can be expressed by the following simplification of Eq. (1):

$$G(\mathbf{x}_B, \mathbf{x}_A, t) + G(\mathbf{x}_A, \mathbf{x}_B, -t) \approx \frac{2}{\rho c} \int_L G(\mathbf{x}_A, \mathbf{x}, -t) * G(\mathbf{x}_B, \mathbf{x}, t)\, d\mathbf{x}, \quad (2)$$

where G denotes now a two dimensional Green's function, which includes the rigid ground surface boundary conditions. Equation (2) applies for impulsive sources (at all $\mathbf{x}$ on L) like blast waves. Suppose now there are uncorrelated noise sources $N(\mathbf{x}, t)$ which are distributed at locations $\mathbf{x}$ on semicircle L, whose wave fields are recorded simultaneously by receiver A and B. An example of such sources could be the microbaroms which are part of the ambient noise field. Since the sources of microbaroms are located on the oceans, the sources do not lie on semicircle L, but on ground level. The microbaroms are refracted by the stratosphere. According to the Huygens principle, these refracted microbaroms can be represented as sources that are located on the semicircle L

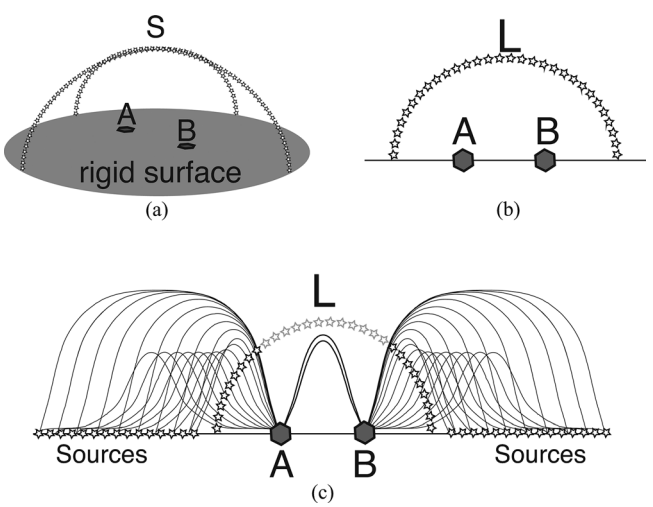

FIG. 1. (a) Two receivers (A and B) on the ground (rigid surface) in a volume with the surface S on which the sources x are located. (b) The integration over the hemisphere above the receivers A and B can be reduced by an integration over the semicircle L. (c) The sources denoted by the black stars on the semicircle L can be represented by stratospherically refracted sources on the ground. The sources in gray are not represented in this example.

(Ruigrok *et al.*, 2010). Figure 1(c) shows an example of how the sources (black stars) on L can represent sources on the ground. The other sources (gray stars) are not represented in this example, but they would not contribute to the result because they are located outside the Fresnel zone (Wapenaar *et al.*, 2010). If all these sources are uncorrelated the ensemble average over their correlations equals $C(t)$, the autocorrelation of N, times a spatial delta function, according to

$$\langle N(\mathbf{x}, -t) * N(\mathbf{x}', t)\rangle = C(t)\delta(\mathbf{x} - \mathbf{x}'), \tag{3}$$

with $\mathbf{x}$ and $\mathbf{x}'$ as locations of two sources, $\langle N(\mathbf{x}, -t) * N(\mathbf{x}', t)\rangle$ indicates an ensemble average, and δ a spatial Dirac impulse on L. In practice, the ensemble averaging is replaced by integrating over sufficiently long time. The observed pressure p, at receiver A and receiver B, consists of all noise sources N convolved with Green's functions

$$p(\mathbf{x}_A, t) = \int_L G(\mathbf{x}_A, \mathbf{x}, t) * N(\mathbf{x}, t) d\mathbf{x} \tag{4a}$$

and

$$p(\mathbf{x}_B, t) = \int_L G(\mathbf{x}_B, \mathbf{x}, t) * N(\mathbf{x}, t) d\mathbf{x}. \tag{4b}$$

The crosscorrelation of the measured ambient noise at receiver A and receiver B can be expressed by crosscorrelating Eqs. (4a) with (4b),

$$\langle p(\mathbf{x}_A, -t) * p(\mathbf{x}_B, t)\rangle = \left\langle \int_L G(\mathbf{x}_A, \mathbf{x}, -t) * N(\mathbf{x}, -t)\, d\mathbf{x} * \int_L G(\mathbf{x}_B, \mathbf{x}', t) * N(\mathbf{x}', t)\, d\mathbf{x}' \right\rangle. \tag{5}$$

If we substitute the spatial ensemble average of the noise sources by the autocorrelation [Eq. (3)] we find

$$\langle p(\mathbf{x}_A, -t) * p(\mathbf{x}_B, t)\rangle = \int_L \int_L G(\mathbf{x}_A, \mathbf{x}, -t) * G(\mathbf{x}_B, \mathbf{x}', t) * C(t)\delta(\mathbf{x} - \mathbf{x}')\, d\mathbf{x}\, d\mathbf{x}'. \tag{6}$$

Using the sift-property of the delta function, we get

$$\langle p(\mathbf{x}_A, -t) * p(\mathbf{x}_B, t)\rangle = \int_L G(\mathbf{x}_A, \mathbf{x}, -t) * G(\mathbf{x}_B, \mathbf{x}, t) d\mathbf{x} * C(t). \tag{7}$$

By convolving Eq. (2) with $C(t)$ the integral in Eq. (2) can be replaced by the left hand side of Eq. (7):

$$\left\{G(\mathbf{x}_B, \mathbf{x}_A, t) + G(\mathbf{x}_A, \mathbf{x}_B, -t)\right\} * C(t) \approx \frac{2}{\rho c}\langle p(\mathbf{x}_A, -t) * p(\mathbf{x}_B, t)\rangle. \tag{8}$$

The right-hand side of Eq. (8) describes the crosscorrelation of ambient noise measured by the receivers A and B on the ground below a moving medium, the atmosphere. According to Eq. (8), this crosscorrelation is equal to the Green's function from $\mathbf{x}_A$ to $\mathbf{x}_B$ plus the time reversed Green's function from $\mathbf{x}_B$ to $\mathbf{x}_A$, convolved with the autocorrelation of the noise. Equation (8) implies that the traveltimes of infrasound between two receivers can be determined by crosscorrelating the ambient noise at these two receivers.

III. MODELING OF THE INFRASOUND PROPAGATION

From here onward we assume the atmosphere is stratified. There are various approaches modeling infrasound propagation through a stratified atmosphere. These are all based on approximations of the wave equation. One of these methods is based on the parabolic equations (Lingevitch *et al.*, 2002). Dependent on the spatial and temporal resolution, this approach can easily lead to high computation costs.

A computationally less intensive method uses the raytracing models. Raytracing simplifies the wave equation by deriving the Hamiltonian equations from the Eikonal equation (Georges, 1971; Cowling *et al.*, 1971). The solution of the Hamiltonian equations is a ray, which indicates the path of infrasound. This high-frequency approximation is possible, since the examined wavelengths are small in relation to the stratified profiles of temperature and wind, and the reflecting surfaces (Blom and Waxler, 2012). Examples of such raypaths are shown in Fig. 2. The raytracing model we implemented solves the Hamiltonian equations numerically with the Runge–Kutta algorithm and uses the effective sound speed approximation. In contrast to existing raytracing models [HARPA (Jones *et al.*, 1986), WASP–3D (Dessa *et al.*, 2005)], which are implemented in spherical coordinates, we implemented the Hamiltonian solver in Cartesian coordinates.

With our raytracing model, it is possible to calculate the raypaths of any emitting angle. However, only rays which connect the sources with the receivers (eigenrays) contribute to the measured pressure. The eigenrays are determined with a least squares approximation of the minimum distance between the receiver and the reflections of the rays on the ground.

While propagating from the source through the atmosphere to the receiver, the infrasound is attenuated and phase shifted. The atmospheric attenuation depends on the

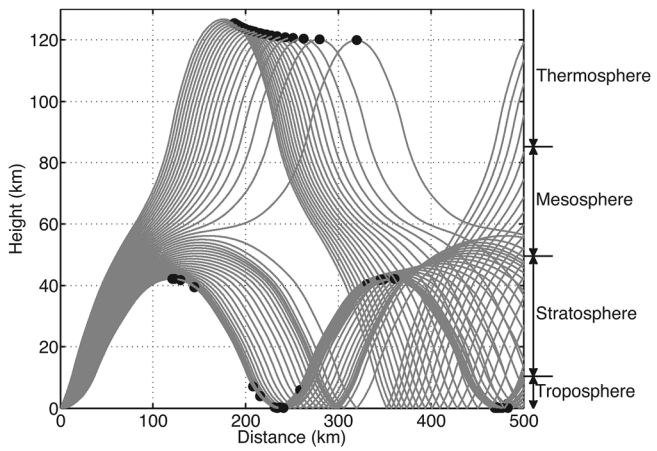

FIG. 2. The rays indicate the path of the infrasound though the atmosphere. The black dots indicate the position of caustics.

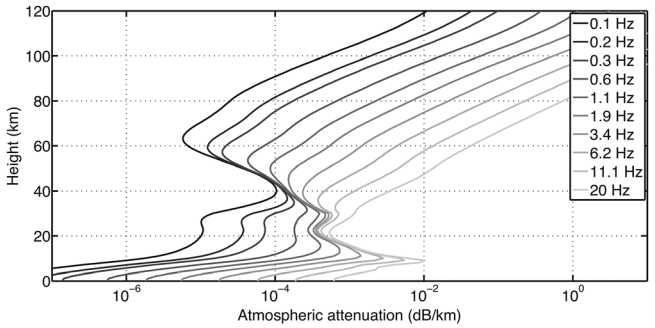

FIG. 3. The atmospheric attenuation as a function of altitude for different frequencies (Picone *et al.*, 2002).

frequency of the infrasound and the density of the atmospheric layer. To calculate the atmospheric attenuation, we use the empirical NRLMSISE–00 model (Naval Research Laboratory Mass Spectrometer and Incoherent Scatter Radar exosphere) (Picone *et al.*, 2002). Figure 3 shows an example of the atmospheric attenuation of different frequencies. The infrasound is additionally reduced by the geometrical spreading since the sound energy is distributed over a larger area. The spreading can be calculated with the Jacobian matrix which takes into account how the ray coordinates are changing when the emitting angle changes. Figure 4 shows an example of geometrical spreading as a function of distance for different emitting angles.

The phase shift depends on caustics. The caustics can be found on the basis of the spreading (Jacobian matrix), since caustics occur when neighboring rays touch (black dots in Fig. 2). First–order caustics cause a phase shift of 90° of the time dependent pressure. Such caustics are taken into account. In caustics the amplitude prediction by raytracing breaks down, since the spreading becomes zero, which result in non-physical predictions of an infinite amplitude (Gilmore, 1993; Pierce, 1989). The time dependent pressure is represented by a source wavelet. The receiver response (also known as barogram) is computed by shifting this wavelet in time and phase, and modifying its amplitude, dependent on the raypath. Two kinds of sources can be generated: blasts and microbaroms. Blast waves occur if a large amount

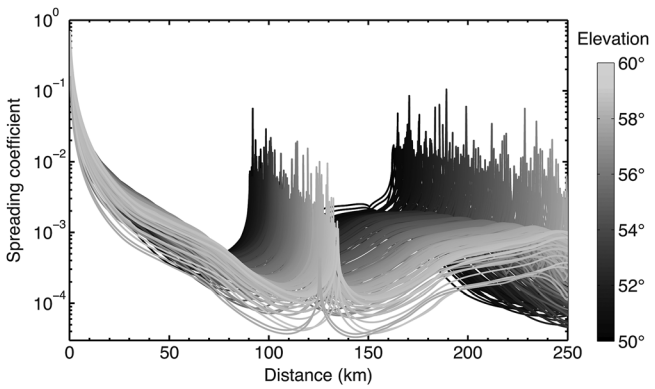

FIG. 4. An example of geometrical spreading as a function of distance. The geometrical spreading depends on the initial elevation angle of the raypath. The geometrical spreading coefficient has a peak at the caustics, since the spreading is zero there.

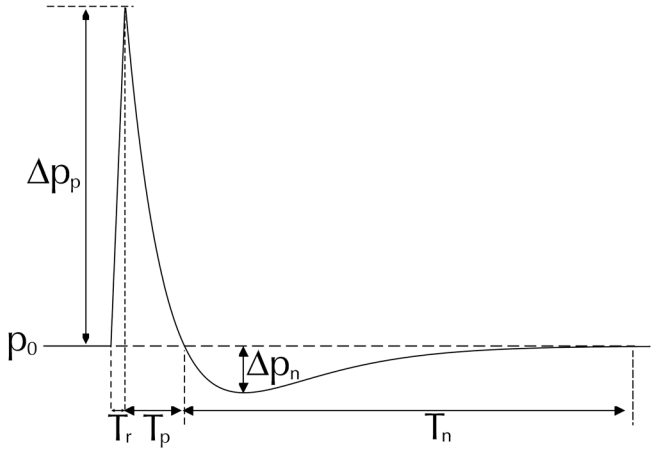

FIG. 5. A blast wave: After a negligible rising time (T_r) the pressure decreases from the positive perturbation (Δp_p) during the positive phase (T_p) until it falls under the normal ambient pressure (Δp_n) during the negative phase (T_n).

of energy is set free in a small volume [e.g., during an explosion (Baker, 1973)], as shown in Fig. 5.

Ground-truth events like explosions, which would generate blast waves are not always available. If there are no events, the receivers measure ambient noise. In the past, ambient noise was considered a disturbance and was ignored. Over the last years, noise has moved more into the focus of scientific interest, since it carries information about the medium through which it propagates. Due to wave-wave interactions in the oceans, acoustic energy is generated that couples with the atmosphere (Brekhovskikh *et al.*, 1973; Waxler and Gilbert, 2006). This energy is due to pressure fluctuations in the ocean and due to the compression of the air by the ocean waves. The ambient noise field in the atmosphere mainly consists of such energy, usually referred to as microbaroms. The empirically well determined spectrum of microbaroms lies between 0.1 and 0.5 Hz and has its maximum at 0.2 Hz (Posmentier, 1967; Donn and Naini, 1973). Figure 6 shows an example of microbaroms, recorded in De Bilt, the Netherlands. Microbaroms can be distinguished from other noise by a strong correlation between different sensors. Note that in this example the sensors are closely spaced and not hundreds of kilometers apart as discussed later in this paper.

IV. NUMERICAL EXPERIMENTS

In this section, we apply infrasonic interferometry to responses of two kinds of sources: blasts and microbaroms. In the first experiment, we model blast waves as line source response and the barograms at two receivers. The traveltimes of the eigenrays between these two receivers are determined using crosscorrelation. The example with blast sources provides a better understanding of the results, because the arrivals related to different raypaths are identifiable in the barograms, although this is an unrealistic set up for blast sources. The second experiment deals with microbaroms emitted from the same source array as in in the previous experiment. Microbaroms are in reality more likely to be encountered simultaneously than blasts.

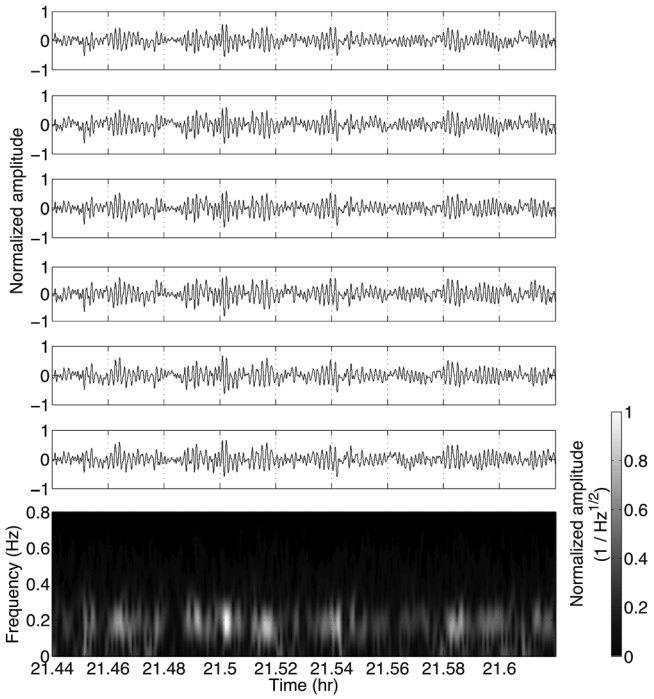

FIG. 6. An example of microbaroms and their spectrum, recorded with six array elements in De Bilt, the Netherlands.

A. Numerical experiment with blast waves

Figure 7 shows the setup of the numerical experiment. 361 sources, with 0.5 km spacing, are used ranging from $x = -90$ to $x = +90$ km. Receiver A and receiver B are located at $\mathbf{x}_A = 210$ km and $\mathbf{x}_B = 430$ km. Note there is only illumination from one side in this setup. However, one-sided illumination suffices to find one of the two Green's function in Eq. (2). For the calculation of the rays, the velocity profiles in the right-hand side of Fig. 7 are used.

Curve c shows the velocity dependent on the temperature and curve c_{ef} the effective velocity dependent on temperature and wind. The effective velocity is obtained by adding the velocity c [Fig. 8(a)] to the projection of the meridional and zonal wind [Fig. 8(b)] in the direction of receiver A and B ($c_{ef} = c + \vec{u} \cdot \vec{n}$, with $\vec{u}$ the wind vector and $\vec{n}$ the vector which directs from receiver A to receiver B). With these velocity profiles, receiver A measures the infrasound which propagates along the eigenrays in Fig. 7(a). Receiver B is reached by the eigenrays plotted in Fig. 7(b). The color refers to the different source locations. For the eigenrays in Fig. 7, the synthetic barograms recorded at each receiver are calculated using the raytracing model described in Sec. III. The result of the two receivers is shown in Fig. 9 for all sources. In this figure, it can be seen that each source has two eigenrays with two different traveltimes to the

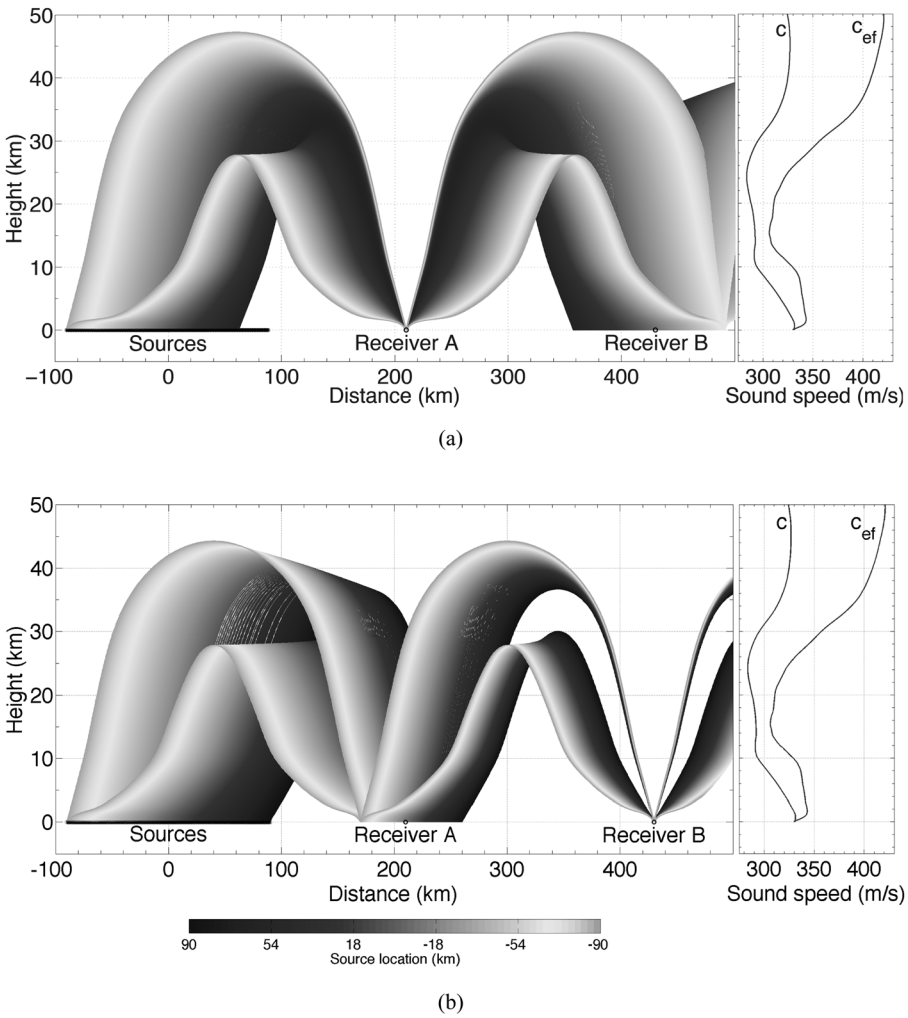

FIG. 7. Receiver A (at 210 km) and B (at 430 km) have different eigenrays. (a) The eigenrays between receiver A and the 361 sources. The color indicates the source location ranging from $x = -90$ km to $x = +90$ km. Not all eigenrays of receiver A reach receiver B. The sources from $x = +63$ km to $x = +90$ km are in the shadow zone of receiver A and do not contribute eigenrays to receiver A. (b) The eigenrays between the sources and receiver B. The corresponding velocity profiles are shown on the right-hand side. Curve c shows the temperature dependent velocity and curve c_{ef} the velocity dependent on temperature and wind.

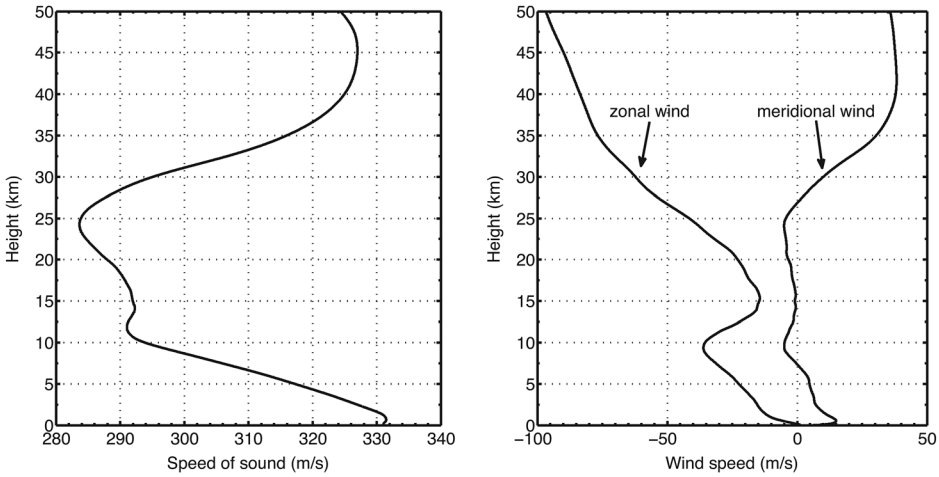

FIG. 8. The sound speed profile (a) and the wind profile (b) used for the calculation of the eigenrays in Fig. 6. The meridional wind is northwardly and the zonal wind eastwardly directed. The effective velocity in Fig. 6 is an addition of the sound speed and the wind in the direction of the sound.

receiver. Infrasonic interferometry, given in Eq. (2), is applied by crosscorrelating the barograms of receiver A and B and summing the result over the sources. Figure 10(a) shows the outcome of the crosscorrelation of each source and Fig. 10(b) shows the summation.

In order to evaluate the result of the interferometry in Fig. 10(b), we compare it with the response computed for a blast wave source located at receiver A and measured at receiver B. This is shown in Fig. 10(c), where we can identify two arrivals: one at 755 s and the second one at 780 s. The arrival at 755 s corresponds to the infrasound refracted at an altitude of 30 km, whereas the one at 780 s corresponds to the rays refracted at an altitude of 40 km (see Fig. 7). These are respectively a fast and slow arrival as also observed by Kulichkov *et al.* (2004); Evers and Haak (2007). The shape of the arrival at 755 s can be explained by minus the autocorrelation of the blast wavelet (Fig. 5). The minus-sign is a result of the two caustics on the 30 km refracted raypath, which cause a phase shift of 180°. By comparing Figs. 10(b) and 10(c), we notice that the result of the crosscorrelation has a clear first arrival at 755 s and a weaker second arrival at 780 s. In Fig. 7(b) it can be seen that the gradient of the effective velocity c_{ef} for the refraction at an altitude of 30 km is much stronger than for the refraction at an altitude of 40 km. If the velocity gradient is stronger, more energy is refracted. Therefore, far more energy will be refracted for the first arrival than for the second arrival. Including more sources and finding more eigenrays may improve the results.

In Fig. 10(b) we also observe several weak events between 730 and 750 s and 785 and 805 s, which do not occur in Fig. 10(c). In order to understand these spurious events, we need to have a closer look at Fig. 10(a), where we can see that they are strongly present for each source. They originate from the crosscorrelation between the two differently refracted raypaths. The spurious event at 730–750 s results from the crosscorrelation of the 40 km refraction at receiver A and the 30 km refraction at receiver B. The spurious event at 785–805 s is the result of the correlation of the 30 km

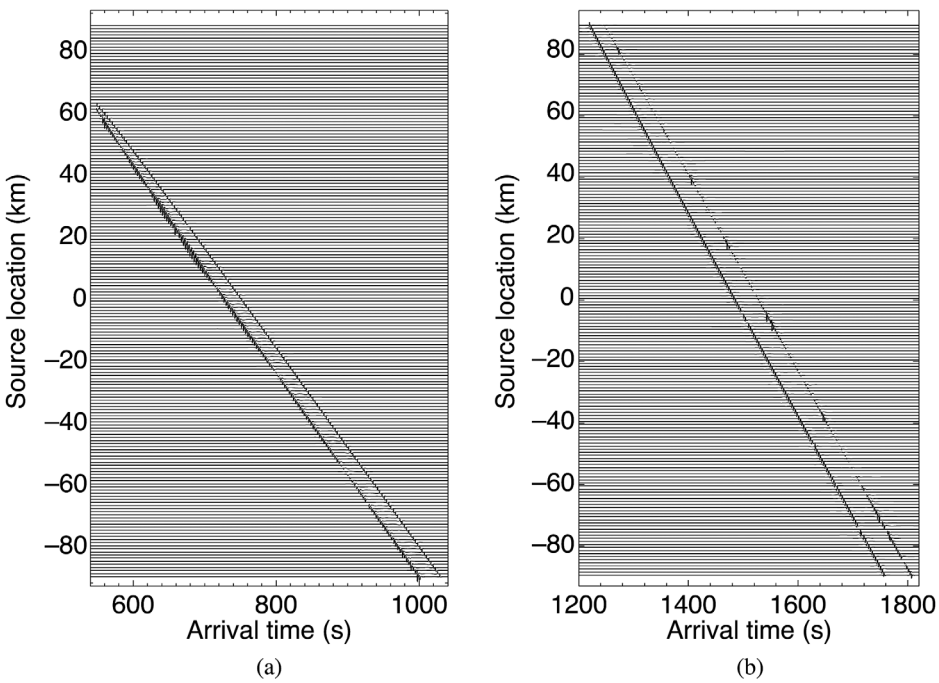

FIG. 9. Each blast wave reaches the receiver via an eigenray (see Fig. 7) with a different traveltime and a different attenuation. (a) Barograms of receiver A. (b) Barograms of receiver B. The amplitude is normalized.

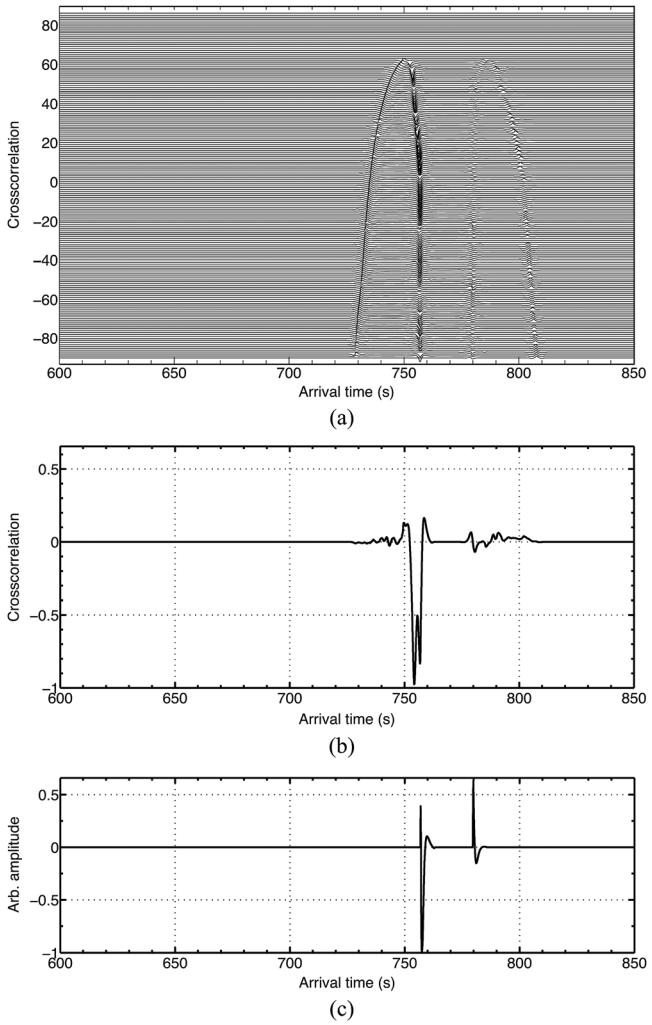

FIG. 10. (a) Crosscorrelations between receiver A and receiver B as given by the integrand in Eq. (2) for each of the 361 source locations. (b) The summations of the different crosscorrelations in (a). (c) The response computed for a blast wave source located at receiver A and measured at receiver B.

refraction at receiver A and the 40 km refraction at receiver B. After summation, the spurious events are suppressed. The spurious events are not completely canceled out, since the sources of the line array (see Fig. 7) cannot represent all sources on the semicircle L [see Fig. 1(c)]. More sources may reach a better coverage of the semicircle L.

B. Numerical experiment with microbaroms

For the numerical experiment with microbaroms, the same source-receiver configuration (Fig. 7) and temperature, wind profiles (Fig. 8) are used as in the previous experiment. In order to simulate microbaroms, random noise is generated and subsequently filtered between 0.1 and 0.5 Hz. Since each source has a different noise signal, all the sources are uncorrelated. The microbaroms propagate along the same eigenrays as the blast waves (see Fig. 7). Figures 11(a) and 11(b) show all the microbaroms due to simultaneously acting noise sources that reach receiver A and B, respectively. In this experiment we also apply infrasonic interferometry given in Eq. (8). In the first step, all microbaroms recorded by receiver A are summed to obtain the simulated measurement shown in Fig. 11(a) bottom. The same procedure is done for receiver B [Fig. 11(b) bottom]. Note: Fig. 11 shows only short time windows, selected from a five-hour simulation. In the second step, the simulated measurements of receiver A and B are crosscorrelated. The result, shown in Fig. 12(a), is evaluated in the same way as in the previous numerical experiment. This is done by comparing it with the response computed for a blast wave source located at receiver A and measured at receiver B [Fig. 12(d)]. In order to find the limits of the crosscorrelation, in practice, we add different noise levels to the microbarom signal predicted at each receiver location. The signal-to-noise ratio is defined as $\mathrm{SNR} = (S/N)^2$, with S the root mean square of the microbaroms and N the root mean square of the added noise. The minimal needed SNR is found by reducing the SNR stepwise. Figure 12(b) shows the

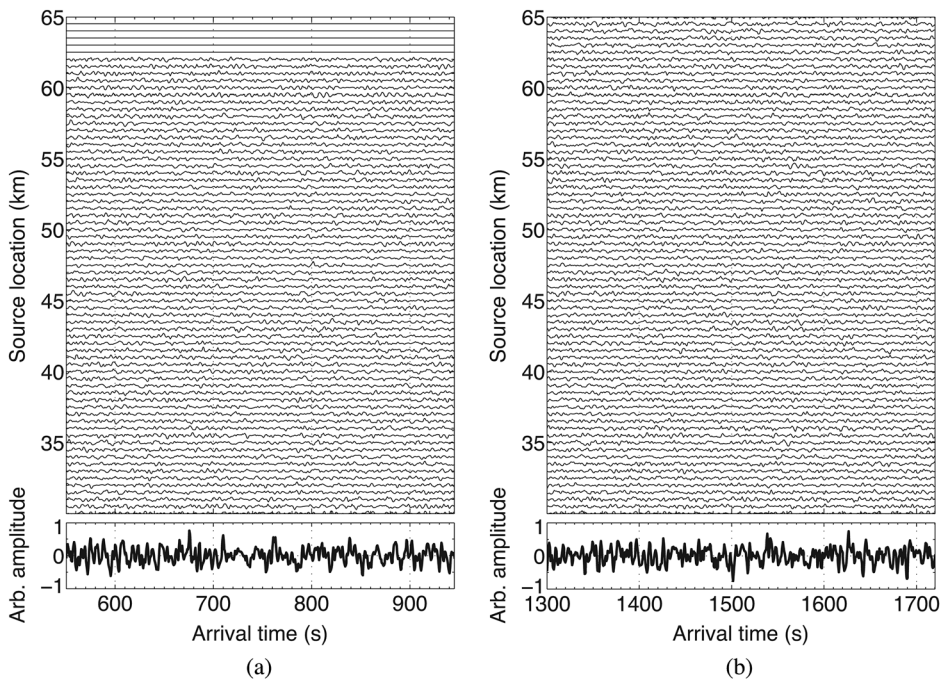

FIG. 11. The simulated measurements are obtained by addition of the microbaroms which reach the receivers. (a) The microbaroms measured at receiver A. (b) The microbaroms measured at receiver B. The figures show a few sources of the simulated 361 sources and a short time window of the simulated five hours.

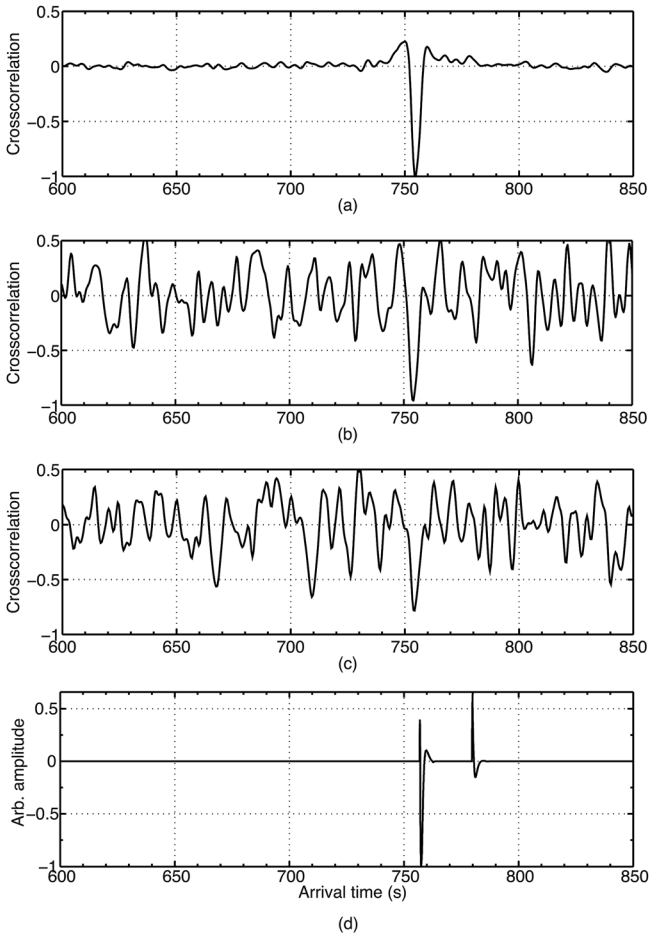

FIG. 12. (a) Crosscorrelations of microbaroms as given in Eq. (7). Five hours of simulated measurements without additional noise (SNR $= \infty$) of receiver A [Fig. 11(a)] and receiver B [Fig. 11(b)] are crosscorrelated. (b) Crosscorrelation of the same simulated data, but with additional noise (SNR $= 0.5$ at receiver A and SNR $= 0.013$ at receiver B). (c) Crosscorrelation of the same simulated data with a SNR $= 0.2$ at receiver A and SNR $= 0.005$ at receiver B. (d) As reference, a blast source at receiver A measured with receiver B.

crosscorrelation of simulated data with SNR $= 0.5$ at receiver A and at receiver B SNR $= 0.013$. The SNR at receiver B is lower because the energy has traveled through the stratosphere. In Fig. 12(c) the crosscorrelation of simulated measurements with a SNR $= 0.2$ at receiver A and SNR $= 0.005$ at receiver B.

In the result of the crosscorrelation, we observe one clear arrival at 755 s, related to the infrasound refracted at 30 km height. The arrival of the 40 km height refraction is not distinguishable because it is masked by noise. The result of the crosscorrelation could be improved by crosscorrelating longer time windows and including more sources. However, a longer time window would have to be based on the assumption of longer constant atmospheric conditions. In the experiment with a SNR of 0.5 we are able to determine the traveltime by crosscorrelation. For a SNR of 0.2 or lower it is hardly possible to resolve the traveltime.

V. CONCLUSIONS

Through numerical experiments, we have verified the theory of infrasonic interferometry and showed that it can be used to estimate the traveltimes of stratospherically refracted waves. We generated synthetic time signals using a raytracing model and taking into account atmospheric attenuation, geometrical spreading and phase shifts due to caustics. Two types of source wavelets were implemented for the numerical experiments: blast waves and microbaroms. We simulated an array of sources and two receivers, which are each reached by eigenrays refracted at 30 and 40 km height. In the first experiment with the blast wave, we were able to estimate the traveltime of the 30 km refraction. The traveltime of the second refraction could be found less clearly, since the velocity gradient at 40 km height is smaller. In the experiment with microbaroms, the traveltime of the first arrival was recovered as well, but the traveltime of the second raypath could not be detected, for the same reason. The results could be improved by including more sources. Nevertheless, the traveltime of the 30 km refraction can be well estimated above a signal-noise-ratio of 0.5 using infrasonic interferometry. This shows that microbaroms can be used in practice to obtain the traveltimes of infrasound through the stratosphere. It depends on the wind and temperature profile which parts of the stratosphere are sampled. In the specific case studied here, arrivals from 40 km altitude did not show up coherently in the crosscorrelation result.

The next step will be the inversion of the traveltimes obtained at many receiver pairs in order to estimate the temperature and wind profiles. For this inversion, the atmospheric conditions of the described raytracing model can be varied. In case the searched temperature and wind profiles are found, the simulated ray propagates from receiver A to B in the estimated traveltime. Therefore, the possible wind and temperature profiles can be estimated in a least squares approximation. A reasonable variation of the atmospheric conditions is based on the empirical orthogonal functions (EOFs) (Williams, 1997; Drob *et al.*, 2010). The EOFs are obtained by applying a principal component analysis to observations of the atmospheric conditions over several years.

In the future, we will apply the proposed methodology to microbaroms, which are measured by the Large Aperture Infrasound Array (LAIA). LAIA has been installed by the Royal Netherlands Meteorological Institute in the framework of the radio-astronomical Low Frequency Array initiative.

ACKNOWLEDGMENTS

We thank Philip Blom and Dr. Roger Waxler of the National Center for Physical Acoustics (NCPA) for supporting us with their knowledge about the geometrical spreading. We also thank Dr. Deyan Draganov for sharing his knowledge about the crosscorrelation of microseisms. This research is funded by the Netherlands Organization for Scientific Research (NWO).

Baker, W. E. (**1973**). *Explosions in Air* (University of Texas Press, Austin, TX), pp. 4–6.

Bensen, G. D., Ritzwoller, M. H., Barmin, M. P., Levshin, A. L., Lin, F., Moschetti, M. P., Shapiro, N. M., and Yang, Y. (**2007**). "Processing seismic ambient noise data to obtain reliable broad–band surface wave dispersion measurements," Geophys. J. Int. **169**, 1239–1260.

Blom, P., and Waxler, R. (**2012**). "Impulse propagation in the nocturnal boundary layer: Analysis of the geometric component," J. Acoust. Soc. Am. **131**, 3680–3690.

Brekhovskikh, L. M., Goncharov, V. V., Kurtepov, V. M., and Naugolnykh, K. A. (**1973**). "The radiation of infrasound into the atmosphere by surface waves in the ocean," Atmos. Oceanic Phys. **9**, 899–907.

Cowling, D. H., Webb, H. D., and Yeh, K. C. (**1971**). "Group rays of internal gravity waves in a wind–stratified atmosphere," J. Geophys. Res. **76**, 213–220, doi: 10.1029/JA076i001p00213.

Dahlman, O., Mykkelveit, S., and Haak, H. W. (**2009**). *Nuclear Test Ban: Converting Political Visions to Reality* (Springer, Berlin), pp. 25–54.

Dessa, J.–X., Virieux, J., and Lambotte, S. (**2005**). "Infrasound modeling in a spherical heterogeneous atmosphere," Geophys. Res. Lett. **32**, L12808, doi:10.1029/2005GL022867.

Donn, W. L., and Naini, B. (**1973**). "Sea wave origin of microbaroms and microseisms," J. Geophys. Res. **78**, 4482–4488, doi: 10.1029/JC078i021p04482.

Draganov, D., Wapenaar, K., Mulder, W., Singer, J., and Verdel, A. (**2007**). "Retrieval of reflections from seismic background–noise measurements," Geophys. Res. Lett. **34**, L04305, doi:10.1029/2006GL028735.

Drob, D. P., Meier, R. R., Picone, J. M., and Garcés, M. A. (**2010**). *Infrared Monitoring for Atmospheric Studies: Inversion of Infrasound Signals for Passive Atmospheric Remote Sensing* (Springer, Dordrecht), pp. 701–731.

Evers, L. G., and Haak, H. W. (**2007**). "Infrasonic forerunners: Exceptionally fast acoustic phases," Geophys. Res. Lett. **34**, L10806, doi:10.1029/2007GL029353.

Evers, L. G., van Geyt, A., Smets, P., and Fricke, J. T. (**2012**). "Anomalous infrasound propagation in a hot stratosphere and the existence of extremely small shadow zones," J. Geophys. Res. **117**, D06120, doi:10.1029/2011JD017014.

Georges, T. M. (**1971**). "A program for calculating three-dimensional acoustic-gravity ray paths in the atmosphere," technical report No. ERL 212–WPL16, National Oceanic and Atmospheric Administration, Boulder, CO, pp. 1–43.

Gilmore, R. (**1993**). *Catastrophe Theory for Scientists and Engineers* (Dover, New York), pp. 319–337.

Godin, O. A. (**2006**). "Recovering the acoustic Green's function from ambient noise crosscorrelation in an inhomogeneous moving medium," Phys. Rev. Lett. **97**, 054301.

Gutenberg, B. (**1939**). "The velocity of sound waves and the temperature in the stratosphere in southern California," Bull. Am. Meteorol. Soc. **20**, 192–201.

Haney, M. M. (**2009**). "Infrasonic ambient noise interferometry from correlations of microbaroms," Geophys. Res. Lett. **36**, L19808, doi:10.1029/2009GL040179.

Jones, R. M., Riley, J. P., and Georges, T. M. (**1986**). "HARPA: A versatile three-dimensional Hamiltonian ray-tracing program for acoustic waves in the atmosphere above irregular terrain," special report, National Oceanic and Atmospheric Administration, Boulder, CO, pp. 1–410.

Kulichkov, S. N., Avilov, K. V., Bush, G. A., Popov, O. E., Raspopov, O. M., Baryschnikov, A. K., ReVelle, D. O., and Whitaker, R. W. (**2004**). "On anomalously fast infrasonic arrivals at long distances from surface explosions," Izv. Russ. Acad. Sci. Atmos. Oceanic Phys., Engl. Transl. **40**, 1–9.

Lalande, J.-M., Sèbe, O., Landès, M., Blanc-Benon, P., Matoza, R. S., Le Pichon, A., and Blanc, E. (**2012**). "Infrasound data inversion for atmospheric sounding," Geophys. J. Int. **190**, 687–701.

Le Pichon, A., Blanc, E., and Drob, D. P. (**2005**). "Probing high-altitude winds using infrasound," J. Geophys. Res. **110**, D20104, doi: 10.1029/2005JD006020.

Lingevitch, J. F., Collins, M. D., Dacol, D. K., Drob, D. P., Rogers, J. C. W., and Siegmann, W. L. (**2002**). "A wide angle and high Mach number parabolic equation," J. Acoust. Soc. Am. **111**, 729–734.

Marcillo, O. E., and Johnson, J. B. (**2010**). "Tracking near-surface atmospheric conditions using an infrasound network," J. Acoust. Soc. Am. **128**, EL14–EL19.

Picone, J. M., Hedin, A. E., Drob, D. P., and Aikin, A. C. (**2002**). "NRLMSISE–00 empirical model of the atmosphere: Statistical comparisons and scientific issues," J. Geophys. Res. **107**, 1468, doi: 10.1029/2002JA009430.

Pierce, A. D. (**1989**). *Acoustics: An Introduction to its Physical Principles and Applications* (Acoustical Society of America, Woodbury, NY), pp. 371–423.

Posmentier, E. S. (**1967**). "A theory of microbaroms," Geophys. J. Int. **13**, 487–501.

Roux, P., and Kuperman, W. A. (**2004**). "Extracting coherent wavefronts from acoustic ambient noise in the ocean," J. Acoust. Soc. Am. **116**, 1995–2003.

Ruigrok, E. N., Campman, X., Draganov, D., and Wapenaar, K. (**2010**). "High resolution lithospheric imaging with seismic interferometry," Geophys. J. Int. **183**, 339–357.

Sabra, K. G., Gerstoft, P., Roux, P., Kuperman, W. A., and Fehler, M. C. (**2005**). "Extracting time-domain Green's function estimates from ambient seismic noise," Geophys. Res. Lett. **32**, L03310, doi:10.1029/2004GL021862.

Shapiro, N. M., and Campillo, M. (**2004**). "Emergence of broadband Rayleigh waves from correlations of the ambient seismic noise," Geophys. Res. Lett. **31**, L07614, doi:10.1029/2004GL019491.

Wapenaar, K. (**2006**). "Nonreciprocal Green's function retrieval by cross correlation," J. Acoust. Soc. Am. **120**, EL7–EL13.

Wapenaar, K., Draganov, D., Snieder, R., Campman, X., and Verdel, A. (**2010**). "Tutorial on seismic interferometry: Part 1—Basic principles and applications," Geophysics **75**, 75A195-75A209.

Wapenaar, K., and Fokkema, J. (**2006**). "Green's function representations for seismic interferometry," Geophysics, **71**, SI33–SI46.

Waxler, R., and Gilbert, K. E. (**2006**). "The radiation of atmospheric microbaroms by ocean waves," J. Acoust. Soc. Am. **119**, 2651–2664.

Weaver, R. L., and Lobkis, O. I. (**2001**). "Ultrasonics without a source: Thermal fluctuation correlations at MHz frequencies," Phys. Rev. Lett. **87**, 134301.

Williams, C. R. (**1997**). "Principal component analysis of wind profiler observations," J. Atmos. Oceanic Technol. **14**, 386–395.